
Unisolver: PDE-Conditional Transformers Are Universal PDE Solvers

Hang Zhou*, Yuezhou Ma*, Haixu Wu[✉], Haowen Wang, Mingsheng Long[✉]

School of Software, BNRist, Tsinghua University, China

{zhou-h23, mayz20, wuhx23, wang-hw21}@mails.tsinghua.edu.cn, {mingsheng}@tsinghua.edu.cn

Abstract

Deep models have recently emerged as a promising tool to solve partial differential equations (PDEs), known as neural PDE solvers. While neural solvers trained from either simulation data or physics-informed loss can solve the PDEs reasonably well, they are mainly restricted to a specific set of PDEs, e.g. a certain equation or a finite set of coefficients. This bottleneck limits the generalizability of neural solvers, which is widely recognized as its major advantage over numerical solvers. In this paper, we present the Universal PDE solver (Unisolver) capable of solving a wide scope of PDEs by leveraging a Transformer pre-trained on diverse data and conditioned on diverse PDEs. Instead of simply scaling up data and parameters, Unisolver stems from the theoretical analysis of the PDE-solving process. Our key finding is that a PDE solution is fundamentally under the control of a series of PDE components, e.g. equation symbols, coefficients, and initial and boundary conditions. Inspired by the mathematical structure of PDEs, we define a complete set of PDE components and correspondingly embed them as domain-wise (e.g. equation symbols) and point-wise (e.g. boundaries) conditions for Transformer PDE solvers. Integrating physical insights with recent Transformer advances, Unisolver achieves consistent state-of-the-art results on three challenging large-scale benchmarks, showing impressive gains and endowing favorable generalizability and scalability.

1 Introduction

Partial differential equations (PDEs) are essential for numerous scientific and engineering problems [8, 2], such as meteorology, electromagnetism and thermodynamics [41]. Since it is usually hard to obtain an analytic solution for PDEs, numerical methods are widely explored [1]. However, these numerical methods often require huge computation costs to generate a precise solution for each PDE. Recently, deep models have empowered many breakthroughs in wide areas [5, 22] and have also been applied to solve PDEs, i.e. neural PDE solvers. Owing to the excellent capability in approximating nonlinear mappings, deep models can learn to fit pre-collected data [19] or physics-informed loss function [33] and generalize in a flash to new samples, offering an efficient way for solving PDEs.

As shown in Figure 1, previous neural solvers involve two different paradigms: physics-informed neural networks (PINNs) [33] and neural operators [19, 44], which train the deep models with formalized PDE loss function and pre-calculated simulation data respectively. However, for the first paradigm, while formalizing the PDE equations as objective functions can ensure a relatively accurate solution, PINNs are hard to generalize to new scenarios and we have to retrain the model for different tasks. As for neural operators, they directly learn from the simulation data, which can generalize better for diverse initial states or conditions than PINNs. Nevertheless, purely based on the training data may be insufficient to guide PDE solving. For example, given a fluid governed by Navier-Stokes equations, the typical task of neural operators is to predict the future based on past observations [19], while different viscosity coefficients and forcing terms will lead to distinct solutions even under the

*Equal Contribution

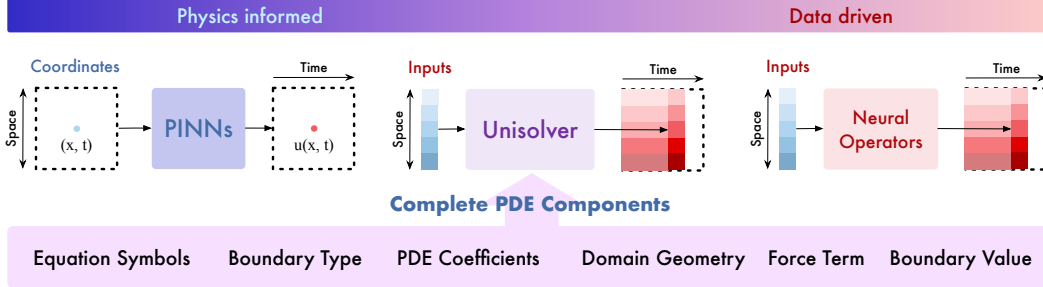


Figure 1: Neural PDE solvers typically consist of two paradigms: physics informed and data driven. Our proposed Unisolver combines data-driven methods with physical insights from complete PDE components in a conditional modeling framework, thereby boosting generalizability and scalability.

same initial state. Thus, due to the omission of PDE information, current neural operators are mainly trained and tested on a specific set of PDEs. Notably, as neural solvers are expected to be efficient surrogates of neural methods, generalization to various PDEs is essential for a practical neural solver.

To tackle the generalization deficiency, several works are proposed by incorporating the PDE information into deep models or training models with a large-scale dataset. For example, message-passing neural PDE solver [3] concatenates the PDE coefficients with inputs. PDEformer [45] formalizes the PDE equation as a computation graph and employs the graph Transformer [46] to aggregate PDE information. Although these methods have explored the potential of training models with both data and PDE information, they fail to support a complete set of PDE information, thereby limiting the generalizability of models in some aspects. As for the other branches, such as DPOT [10], they just scale up the training sets with diverse PDEs and expect the generalizability emerges from large data and parameters. However, without the complete PDE information, it is theoretically impossible to generate a correct solution because what the models essentially perform is fitting an incomplete data distribution, so it is hard to expect satisfactory generalizability.

Going beyond prior methods, as shown in Figure 1, this paper presents Unisolver as a Universal PDE solver. Concretely, Unisolver takes the advantages from both data-driven and physics-informed paradigms and empowers Transformer with favorable PDE generalizability by introducing complete physics information as conditions. Instead of simply scaling up data and parameters, we start from the theoretical analysis of PDE solving and conclude with a complete set of PDE components. Further, drawing inspiration from the mathematical structure of PDEs, we propose to classify PDE components into domain-wise and point-wise categories according to their effect on the final solution and aggregate them as two types of deep PDE conditions. Afterward, to capture the special influence of different condition types on the hidden input feature, we separate the Transformer representation into two subspaces and integrate these deep conditions into Transformer in a decoupled way. We conduct extensive experiments on our own generated dataset and two large-scale benchmarks with various PDE conditions, where Unisolver achieves consistent state-of-the-art with sharp relative gains. Overall, our contributions are summarized as follows:

- We introduce Unisolver as a conditional Transformer architecture utilizing embedded PDE information completely, marking the first demonstration of the potential of the canonical Transformer as a scalable backbone for solving multiple PDEs with diverse conditions.
- Motivated by the mathematical structure of PDEs, we classify universal PDE conditions into domain-wise and point-wise categories, which further derives a decoupled conditioning mechanism incorporating designs for introducing PDE conditions to deep representations.
- Unisolver achieves consistent state-of-the-art performances across three large-scale benchmarks with impressive relative gains and presents favorable generalizability and scalability.

2 Related Work

2.1 Neural PDE Solvers

Previous neural PDE solvers can be roughly categorized into the following two paradigms. The first paradigm is physics-informed neural networks (PINNs) [33], which optimize the deep model

by formalizing the PDE equations as objective functions. During training, the model outputs and gradients will gradually satisfy the targeted PDE, thereby successfully instantiating the solution as a deep model. However, PINNs are usually hard to generalize to unseen PDEs, limiting their applications in broader practice [41]. Another booming direction is neural operators, which learn from extensive data to approximate functional dependence between input and output Banach spaces [25, 15]. Among various neural operators, FNO [19] and its variants [18, 32, 42] are popular and well-established. FNO [19] effectively approximates the kernel integral operator in the frequency domain through Fourier transformation. Besides, LSM [43] generalizes the classical spectral method in latent space to avoid the curse of dimensionality. Recently, given the impressive progress achieved by Transformers [40], they have also been applied to solve PDEs. However, due to the quadratic complexity of the attention mechanism, the main challenge in applying Transformers is defining the tokens used to compute attention in PDE-solving tasks. OFormer [16] and GNOT [11] treat each mesh point as a token and utilize the linear Transformer to avert the complexity problem. Factformer [17] axially factorizes the attention block to boost the model efficiency. Recently, Transolver [44] proposes to learn the intrinsic physical states as tokens behind the input meshes. Despite the success of neural operators, they are only tested on the dataset that contains one certain PDE. The effectiveness of these methods under large and diverse datasets has not been fully explored.

2.2 Generalizable PDE Solvers

In addition to model architectures, the generalizability of neural solvers, the major advantage over numerical solvers, has also been explored. The research mainly lies in the following two directions.

Incorporating PDE information To guide the PDE-solving process, the PDE information has been introduced to deep models. For example, PINO [20] imposes explicit equation constraints at a higher resolution to assist the learning of neural operators. CAPE [36] embeds PDE coefficients to adapt neural solvers to unseen PDE parameters. Prose [21] and PITT [23] tokenize PDEs and embed the mathematical expressions to make the transformer backbone aware of the underlying physics. PDEformer [45] represents the symbolic form of equations as a graph and the numeric components as nodes to optimize the processing of complex interactions between symbolic and numeric information. Still, all of these methods, while incorporating equation information, do not leverage the mathematical structure of PDEs for complete and categorized embedding or integrating the meanings of equation symbols within the context of natural language. In contrast, Unisolver applies powerful Large Language Models (LLMs) [38] to semantically embed the equation symbolic information and categorize the complete equation conditions based on mathematical insights, thereby better at modeling intricate physical correlations.

Large-scale pre-training As a vital cornerstone of deep learning [4, 12], recent research has also started to explore the effectiveness of large-scale training in solving PDEs. In [35], authors examined the scaling capabilities and transfer learning behaviors of FNO on three time-independent equation families. MPP [27] proposes an auto-regressive strategy to pre-train on a broad fluid mechanics-oriented benchmark. DPOT [10] enhances MPP with the denoising method and pre-trains a Fourier transformer on massive PDE data comprised of 12 datasets. PDEformer [45] focuses on a 1D time-dependent PDE family and pre-trains a graph transformer on 3M samples under various equation conditions. However, most of the existing methods fall short in effectively and completely integrating PDE conditions. This will be well addressed by Unisolver in a natural and insightful way.

3 Unisolver

To tackle the incapability in generalization behind neural PDE solvers, we deeply dive into the PDE-solving process and present Unisolver to model the intricate interactions between initial observations and complete equation components, leading to a novel PDE-conditional Transformer model.

Problem setup Let domain $\mathcal{D} \subset \mathbb{R}^d$ be a bounded continuous set and $\mathcal{M} = \{x_1, \dots, x_n\}$ be a n -point discretization of \mathcal{D} , recording the coordinate information of each point. Assume that we have observations of initial conditions \mathbf{X} as input and target quantities \mathbf{Y} as output on mesh \mathcal{M} with governed PDE components \mathbf{C}_{PDE} (e.g. equation symbols, coefficients, etc) for each observation pair. The PDE-solving task is to approximate the input-PDE-output mapping $G : (\mathbf{X}, \mathcal{M}, \mathbf{C}_{\text{PDE}}) \rightarrow \mathbf{Y}$. For instance, in fluid prediction, we need to predict the future vorticity field based on the initial field, observation grid, as well as PDE equations, viscosity coefficients, and force terms.

3.1 Complete PDE Components

To enable complete modeling of the PDE, we attempt to incorporate all the underlying components that affect final solutions into neural solvers. Here, we elucidate the complete PDE components by considering the classical *vibrating string equation* with fixed endpoints as a motivating example:

$$\partial_{tt}u - a^2\partial_{xx}u = f(x, t), \quad (x, t) \in (0, L) \times (0, T), \quad (1a)$$

$$u(0, t) = 0, \quad u(L, t) = 0, \quad t \in (0, T], \quad (1b)$$

$$u(x, 0) = \phi(x), \quad \partial_t u(x, 0) = \psi(x), \quad x \in [0, L]. \quad (1c)$$

The equation formulation precisely models the physical laws governing string vibrations. In this PDE, the coefficient a is determined by physical properties, such as tension and linear density, while f represents the external force that drive the vibrations of the string. The domain geometry spans the range $[0, L] \times [0, T]$, which affects the mesh discretization in numerical solving, especially for irregular geometries. In addition, Equation (1b) sets Dirichlet boundary conditions at the endpoints, maintaining zero displacement throughout the vibration period. Equation (1c) specifies the string’s position $\phi(x)$ and velocity $\psi(x)$ at time zero. These complete equation components theoretically determine a unique solution. In the following theorem, we dive into the PDE-solving process and explore how the equation components affect the final solution.

Theorem 3.1 (The connections between PDE solutions and complete PDE components). *The analytical solution of equation (1a) with boundary conditions (1b) and initial conditions (1c) is*

$$u(x, t) = \frac{1}{2} \underbrace{(\Phi(x + at) + \Phi(x - at))}_{\text{Initial position}} + \frac{1}{2a} \underbrace{\int_{x-at}^{x+at} \Psi(\xi) d\xi}_{\text{Initial velocity}} + \frac{1}{2a} \int_0^t d\tau \underbrace{\int_{x-a(t-\tau)}^{x+a(t-\tau)} F(\xi, \tau) d\xi}_{\text{Force}}, \quad (2)$$

where $\Phi(x)$, $\Psi(x)$ and $F(x, t)$ are odd, periodic functions with period $2L$ defined on the upper half plane, extended from $\phi(x)$, $\psi(x)$ and $f(x, t)$. The *boundary conditions* will be explicit by extending the equation to the upper half plane and solving it by operator splitting and characteristic lines.

Proof. See Appendix B for the explicit solution and the complete proof. \square

From the analytical solution of the simple motivating example, we pinpoint that the PDE is solved under the complex interactions between a series of equation components. Specifically, the coefficient a exerts a consistent influence over the domain, while the impact of the external force f is imposed point-wisely. This distinction inspires us to classify the PDE components into two categories, *domain-wise* and *point-wise*, which better capture the intricate interactions.

As presented in Table 1, the equation formulation is a domain-wise component due to its consistency across all locations. Domain geometry is a point-wise component since it is represented by a binary mask and each point’s inclusion is determined individually. Boundary conditions are slightly more complex to handle. Commonly used boundary conditions

are divided into two main types: periodic boundary conditions and Robin (non-periodic) conditions. We classify the boundary condition type as a domain-wise component and the specific boundary value functions with zero values at non-boundary points as point-wise components.

Table 1: Concrete categorization of complete PDE components: domain-wise and point-wise.

Domain-wise components	Point-wise components
Equation formulation	External force
Equation coefficient	Domain geometry
Boundary condition type	Boundary value function

3.2 Universal Components Embedding

As described in Section 3.1, PDE solutions can be obtained by intricate interactions between initial conditions and multiple equation components classified into two categories. In previous works, these components are coarsely and incompletely included as conditions by using them to modulate the input observations. In this paper, we will elaborate on how Unisolver finely and completely embeds all equation components (Table 1) into deep PDE conditions based on our insights from the analysis.

Equation formulation Since the mathematical symbols convey rich mathematical information, we utilize a Large Language Model (LLM) for symbolic embedding. Specifically, we employ the

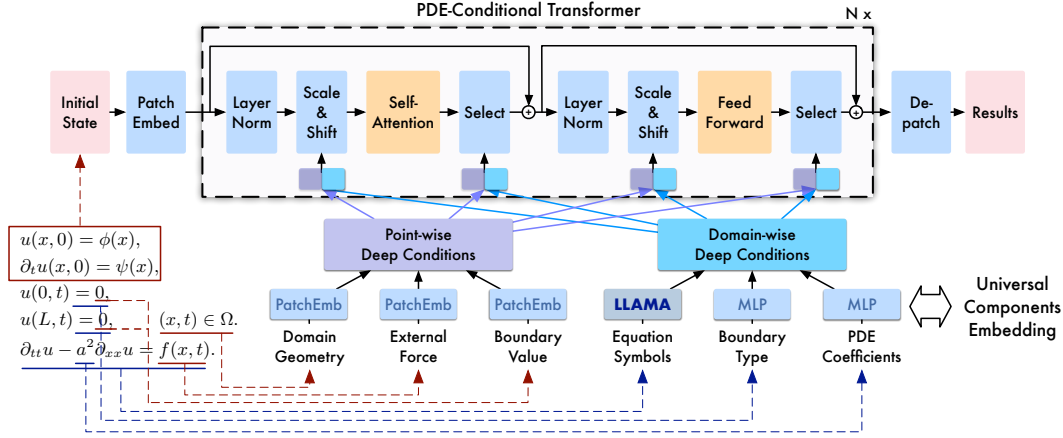


Figure 2: Overview of Unisolver. We universally embed all PDE components into deep conditions and employ a conditional Transformer to aggregate deep conditions in the decoupled subspace.

recently released LLaMA 3 8B model² to embed the equation formulation, leveraging its symbolic understanding ability from pre-training on 15 TB language tokens. The input to the LLM is the LaTeX code of the equation formulation. For example, the string vibration equation is prompted as

Prompt: `"\partial_{tt} u - a^2 \partial_{xx} u = f(x,t)"`

Then we take the output of the last Transformer block of the LLM and compute the mean across the sequence dimension, resulting in a 4096-dimensional embedding for each equation. Since we embed the complete equation components separately, we represent the other components, e.g. coefficients and external force, as symbols in the prompt rather than using their corresponding values. After LLM embedding, the hidden formulation is encoded by a two-layer MLP to obtain deep conditions.

Other components Other domain-wise components encompass coefficients, which are real-valued vectors, and boundary types, which are analogous to class labels. Thus we embed them using two MLP layers with in-between SiLU activation function [7]. Moreover, point-wise components include external force, binary geometry mask, and boundary value functions, which are physical fields observed on mesh \mathcal{M} . We employ the same patchify method used for the input observations, transforming them into token sequences and linearly mapping each token to a deep representation.

Deep condition consolidation After universal components embedding, deep conditions within the same category are aggregated together to consolidate their influence. This strategy is advantageous because it prevents excessive separation of component conditions that could weaken the model’s expressive capabilities, and thus will enhance representation learning for PDE solving via pre-training. Additionally, it allows for easy adaptation to new conditions in downstream tasks by only requiring finetuning a zero-initialized MLP.

3.3 PDE-Conditional Transformer

We propose a conditional Transformer to adaptively fuse these deep conditions embedded from the equation components, empowered by the projections of input observations in decoupled subspaces.

Subspace decoupling We split the hidden inputs along the feature dimension guided by a hyperparameter, the domain-wise condition ratio α , which is set to 0.5 by default. This ratio determines the subspace for domain-wise conditions with dimension $d_{\text{domain}} = \lfloor \alpha \cdot d_{\text{feature}} \rfloor$, while the remaining subspace of dimension $d_{\text{point}} = d_{\text{feature}} - d_{\text{domain}}$ is used by point-wise conditions. When combined with multi-head attention [40], subspace decoupling is equivalent to assigning some heads to learn the impact of domain-wise conditions while others focusing on point-wise conditions. This leads to improved representation learning for both categories, and minimized interference across the subspace.

Deep condition aggregation We utilize MLPs to individually project domain-wise conditions and point-wise conditions into the corresponding subspace. After projection, domain-wise conditions are

²<https://ai.meta.com/blog/meta-llama-3/>

repeated along the sequence dimension to match the length of hidden tokens and ensure consistent physical guiding along the entire sequence. The transformed conditions convey both token-wise and feature-wise information, which are then integrated adaptively by aggregation functions.

As shown in Figure 2, we aggregate conditions either before or after the attention and feedforward modules. Inspired by recent conditional Transformer advances like DiT [29] and other conditional normalization approaches [28, 30], we take the aggregation paradigm to finely capture the intricate correlations between hidden inputs of initial observations and deep equation conditions. Specifically, we scale and shift the hidden inputs based on the conditions. After passing through the Transformer modules, we use the conditions to softly select whether this information should be retained.

Overall design We embed input of initial observations \mathbf{X} using a patchification layer similar to ViT [6] to obtain the input embeddings \mathbf{X}^0 , and embed the complete PDE equation components \mathbf{C}_{PDE} following Section 3.2 to obtain deep conditions $\mathbf{C}_{\text{domain}}$ and $\mathbf{C}_{\text{point}}$. Suppose there are N layers in the PDE-conditional Transformer architecture, the n -th layer of Unisolver can be formalized as follows:

$$\begin{aligned} \mathbf{I}_{\text{op}} &= \text{Concat}(\text{MLP}(\mathbf{C}_{\text{domain}}).\text{repeat}, \text{MLP}(\mathbf{C}_{\text{point}})), \\ \mathbf{X}^{n-\frac{1}{2}} &= \mathbf{I}_{\text{select}} \odot \text{Self-Attention}(\mathbf{I}_{\text{scale}} \odot \text{LayerNorm}(\mathbf{X}^{n-1}) + \mathbf{I}_{\text{shift}}) + \mathbf{X}^{n-1}, \\ \mathbf{I}'_{\text{op}} &= \text{Concat}(\text{MLP}'(\mathbf{C}_{\text{domain}}).\text{repeat}, \text{MLP}'(\mathbf{C}_{\text{point}})), \\ \mathbf{X}^n &= \mathbf{I}'_{\text{select}} \odot \text{FeedForward}(\mathbf{I}'_{\text{scale}} \odot \text{LayerNorm}(\mathbf{X}^{n-\frac{1}{2}}) + \mathbf{I}'_{\text{shift}}) + \mathbf{X}^{n-\frac{1}{2}}, \end{aligned} \tag{3}$$

where $\forall \text{op} \in \{\text{scale}, \text{shift}, \text{select}\}$, $n \in \{1, \dots, N\}$, and \mathbf{X}^n is the output of the n -th layer. As the PDE components have a crucial impact on the scale of the output, we apply conditional scale and shift operations before a linear projection on \mathbf{X}^N to obtain the final output \mathbf{Y} , as shown in Figure 2.

While our model takes similar aggregation mechanisms as DiT, it includes several PDE-inspired differences. First, we do not use a diffusion model because PDE solving demands accuracy more than diversity. Second, our conditions are drawn from equation components with physical insights, unlike the timesteps and text descriptions typically used in generative models [13]. Third, our conditions are not confined to scalar values; instead, we decouple the feature space and leverage point-wise conditions special to PDEs to learn interactions between initial observations and PDE components.

4 Experiments

We conduct extensive experiments to evaluate Unisolver on a challenging, self-generated Heterogeneous 2D Navier-Stokes Equations dataset and two large-scale benchmarks proposed by PDEformer [45] and DPOT [10], covering a broad range of PDEs and diverse generalization scenarios.

Benchmarks As summarized in Table 2, our experiments involve three large-scale datasets and numerous equation conditions in both 1D and 2D spaces. Specifically, we generate the HeterNS dataset as an extension for the NS dataset of FNO [19], including multiple coefficients and forces. PDEformer proposes a large-scale dataset with 3M samples of structured 1D PDEs and evaluates the pre-trained model on PDEBench [37]. DPOT collects 12 datasets from FNO [19], PDEBench [37], PDEArena [9] and CFDBench [26] for diversity. More details can be found in Appendix C.

Table 2: Summary of benchmarks. \checkmark indicates the PDE component will change among different samples, while \times refers to unchanged ones. Unisolver can handle all kinds of changed components.

Benchmarks	#Dim	#Resolution	# Samples	#Size	Symbols	Coefficient	Force	Geometry	Boundary
HeterNS	2D+Time	(64,64,10)	15k	4.6 GB	\times	\checkmark	\checkmark	\times	\times
PDEformer [45]	1D+Time	(256,100)	3M	300 GB	\checkmark	\checkmark	\checkmark	\times	\checkmark
DPOT [10]	2D+Time	(128,128,10)	74.1k	384 GB	\checkmark	\checkmark	\checkmark	\checkmark	\checkmark

Baselines We compare Unisolver with three advanced baselines on the HeterNS dataset to demonstrate its generalizability under varied conditions, including classical ViT [6], FNO [19] and current state-of-the-art neural operator Factformer [17]. Specifically, to ensure a fair comparison, we also include the additional PDE components used in Unisolver to these baselines by concatenating them with inputs. We also compare Unisolver with other generalizable solvers: PDEformer [45] and DPOT [10] on pre-training loss and zero-shot and fine-tuning settings.

Table 3: Performance comparison on HeterNS with different viscosity coefficients and fixed force frequency coefficient $\omega = 2$. Relative L2 is recorded. Promotion refers to the relative improvement over the second-best method. "ID" means in-distribution case and "OOD" means the out-of-distribution.

HeterNS	Viscosity ν	8e-6	1e-5	3e-5	5e-5	8e-5	1e-4	3e-4	5e-4	8e-4	1e-3	2e-3
	Params	OOD	ID	OOD								
FNO	4.7M	0.0702	0.0669	0.0373	0.0225	0.0141	0.0114	0.0088	0.0031	0.0084	0.0011	0.2057
Factformer	9.4M	0.0489	0.0438	0.0489	0.0128	0.0297	0.0064	0.1386	0.0018	0.0631	0.0010	0.3207
ViT	4.8M	0.0458	0.0432	0.0353	0.0206	0.0119	0.0098	0.0100	0.0031	0.0174	0.0015	0.1878
Unisolver	4.1M	0.0336	0.0321	0.0178	0.0094	0.0064	0.0051	0.0066	0.0015	0.0096	0.0008	0.1504
Promotion	-	26.6%	25.7%	49.6%	26.6%	46.2%	20.3%	34.0%	16.7%	-	20.0%	19.9%

Table 4: Comparison (relative L2) on HeterNS with varied force and fixed viscosity $\nu = 10^{-5}$.

HeterNS	Force ω	0.5	1	1.5	2	2.5	3	3.5
	Params	OOD	ID	OOD	ID	OOD	ID	OOD
FNO	4.7M	1.110	0.0640	0.1742	0.0661	0.1449	0.1623	0.2974
Factformer	9.4M	0.9998	0.0326	0.1110	0.0438	0.1243	0.0803	0.2257
ViT	4.8M	0.7900	0.0348	0.1412	0.0432	0.1240	0.1000	0.2080
Unisolver	4.1M	0.0980	0.0244	0.0770	0.0321	0.0720	0.0720	0.1740
Promotion	-	87.6%	25.2%	30.6%	25.7%	41.9%	10.3%	16.4%

Implementations For fairness, in the HeterNS dataset, all the methods are trained with relative L2 loss for 300 epochs, using the ADAM [14] optimizer with an initial learning rate of 0.0005 and a cosine annealing learning rate scheduler [24]. The batch size is set to 60. In the large-scale PDEformer and DPOT benchmarks, we follow their training strategies to compare unbiasedly. We adopt relative L2 as the evaluation metric. See Appendix D for thorough implementation details.

4.1 Heterogeneous 2D Navier-Stokes Equation (HeterNS)

Setups To test the model performance on diverse varied coefficients, we generate HeterNS, which is extended from the widely used 2D NS dataset [19]. The original 2D NS dataset only contains the fixed viscosity coefficient and external force for each task, which cannot be used to evaluate the effectiveness of the model in handling varied equation components. In contrast, HeterNS involves five different viscosity coefficients and three different external force within the family of trigonometric functions, resulting in 15 different equation component pairs and 15k samples. Specifically, HeterNS considers viscosity coefficient $\nu \in \{10^{-5}, 5 \times 10^{-5}, 10^{-4}, 5 \times 10^{-5}, 10^{-3}\}$ and force frequency coefficient $\omega \in \{1, 2, 3\}$. In this benchmark, we evaluate the in-distribution fitting ability and out-of-distribution generalization performance on different viscosity ν and force ω .

Results As shown in Tables 3-4, Unisolver achieves the best performance on 10 of 11 tasks, covering both ID and OOD settings. Notably, for external force generalization, Unisolver beats other methods more significantly in OOD conditions (average 44.1%) than ID conditions (average 20.4%), demonstrating the effectiveness of our design in capturing generalizable physics relations between external force and model inputs. Even though we explicitly concatenate the condition information with the model inputs, without special designs for PDE conditions, most advanced neural operators perform unremarkably on HeterNS. Specifically, all neural operators fail to solve the case of $\omega = 0.5$ in Table 4, highlighting the benefits of our conditional Transformer design in learning generalizable features. We also include experiments in Appendix E.1, where both ν and ω are OOD. Unisolver still achieves considerable improvement (average 41.3%) on this challenging double OOD setting.

4.2 1D Time-dependent PDEs

Setups Proposed by PDEformer [45], this benchmark contains 3 million high-quality 1D time-dependent PDE samples with varied equation symbols, coefficients, forces, and boundary conditions for pre-training, with periodic and Robin boundary conditions each comprising half of the dataset. The input for the pre-training task consists of all the PDE components, and the output is the full space-time field. Similar to PDEformer, we utilize an adapted version of Poly-INR [34] to decode

Table 5: Performance (relative L2) comparison of pre-training and finetuning on 1D time-dependent PDEs. PDEformer-L means the large version of PDEformer. FT-100 means finetuning 100 epochs.

1D Time-dependent PDEs	Tasks	Pretrain		Burgers			Advection
	Params	Periodic	Robin	$\nu = 0.1$	$\nu = 0.01$	$\nu = 0.001$	$\beta = 0.1$
PDEformer-L	22M	0.0211	0.0238	0.00744	0.0144	0.0393	0.0178
Unisolver	19M	0.0107	0.0108	0.00513	0.00995	0.0299	0.0138
Promotion	-	49.3%	54.6%	31.0%	30.9%	23.9%	22.5%
PDEformer-L (FT-100)	22M	-	-	0.00364	0.0112	0.0331	0.00975
Unisolver (FT-100)	19M	-	-	0.00105	0.00474	0.0170	0.00420
Promotion	-	-	-	71.2%	57.7%	48.6%	59.6%

Table 6: Performance comparison across 12 pre-training datasets. Relative L2 ($\times 10^{-2}$) is recorded.

2D Mixed PDEs	Equations Params	FNO-NS- ν			PDEBench-CNS-(M, ζ)				DR	SWE	PDEArena-NS		CFDBench-NS	Mean
		1e-5	1e-4	1e-3	(1, 0.1)	(1, 0.01)	(0.1, 0.1)	(0.1, 0.01)			-	-		
DPOT-S	30M	5.53	4.42	1.31	1.53	3.37	1.19	1.87	3.79	0.66	9.91	31.6	0.70	5.50
Unisolver	33M	4.17	3.36	0.61	1.23	2.89	1.01	1.59	4.39	0.45	6.87	27.4	0.54	4.54
Promotion	-	24.6%	24.0%	53.4%	19.6%	14.2%	15.1%	15.0%	-	31.8%	30.7%	13.3%	22.9%	17.5%
DPOT-S-FT	30M	4.49	3.42	0.68	1.52	2.11	1.50	1.51	1.71	0.22	8.92	29.0	0.44	4.63
Unisolver-FT	33M	3.82	2.79	0.31	0.95	1.99	1.01	1.34	1.37	0.20	6.67	26.8	0.47	3.98
Promotion	-	14.9%	18.4%	54.4%	37.5%	5.69%	32.6%	11.3%	19.8%	9.1%	25.2%	7.6%	-	14.0%

the PDE solution from the features extracted by Unisolver. After pre-training, the pre-trained model is evaluated using Burgers equation and Advection equation from PDEBench[37], where the PDE coefficients fall within the distribution of the pre-training data. Concretely, we recorded the results for zero-shot on Burgers and Advection, and finetuning on the these two dataset after 100 epochs.

Results Table 5 presents that the pre-training performance of Unisolver is significantly better than that of PDEformer-L on both periodic and Robin boundary conditions, which indicates that our design of incorporating PDE conditions is more effective than the computational graph utilized by PDEformer in modeling complex distributions. Additionally, UniSolver achieves better performance in zero-shot evaluations on downstream tasks, with an average improvement of 27.1% over PDEformer-L. Furthermore, fine-tuning on downstream tasks yields even more pronounced improvements for Unisolver (average 59.3%), highlighting its larger model capacity despite relatively fewer parameters.

4.3 2D Mixed PDEs

Setups This benchmark is gathered by DPOT [10], which involves 12 datasets from four different sources, covering a wide range of PDEs. For conciseness, we adopt the “source-PDE” to record different tasks in Table 6, e.g. FNO-NS. The second row lists the primary conditions considered for each dataset. For example, 1e-5 represents the viscosity coefficient $\nu = 10^{-5}$. Unlike the well-balanced data in PDEformer, these datasets exhibit significant imbalance among different conditions. To address this issue, we adopted the balanced data sampling method used in DPOT, but it still presents thorny challenges in tackling intricate and multifarious PDE samples.

Results We pre-trained Unisolver with 33M parameters to compare with DPOT-S, the small version of DPOT. As shown in Table 6, our method outperforms DPOT in 11 out of 12 datasets except for a small dataset DR whose relative L2 is less than 5%, verifying the effectiveness of our design in modeling complex conditions. After 200 epochs of fine-tuning on each dataset, Unisolver achieves a reduction in error of more than 12% compared with zero-shot results, demonstrating its ability to extract useful knowledge from complex pre-training datasets. These results further highlight the potential of Unisolver for serving as a foundation PDE solver.

4.4 Model Analysis

Ablations We conduct detailed ablations on 1D time-dependent PDEs of 50k samples, with 50% periodic and 50% Robin boundaries. From Table 7, we have the following observations. Firstly, without equation symbols, model performance on all tasks will drop consistently, demonstrating the necessity of introducing symbolic information. However, the choice of LLM has minimal

Table 7: Ablations on different LLM choices, removing our designs (W/o), and replacing domain-wise or point-wise conditions from our design to input concat (Concat-D and Concat-P).

L2RE Dataset	Different LLMs		W/o		Condition Modeling		Ours
	T5 [31]	LLaMa-2 [39]	LLM Embedding	Subspaces	Concat-D	Concat-P	
Pretrain-periodic	<u>0.0329</u>	<u>0.0329</u>	0.0358	0.0331	0.0433	0.0327	0.0330
Pretrain-robin	0.0223	<u>0.0224</u>	0.0232	0.0243	0.0427	0.0306	0.0223
Burgers $\nu = 0.01$	0.0664	0.0647	0.0692	0.0675	0.0950	0.0769	<u>0.0659</u>

impact on performance, probably due to the limited ablation data and the prompt design. Secondly, removing subspace decoupling impairs the performance on robin boundaries more significantly for the insufficient modeling of point-wise conditions influenced by domain-wise conditions. Thirdly, replacing the conditional modeling with directly concatenating conditions to the initial inputs severely harms relation learning, further highlighting the advantages of our design.

Case study To provide an intuitive comparison, we provide showcases on the HeterNS benchmark in Figure 3. First, all the presented trajectories are generated from the same initial condition but exhibit distinct final fields, underscoring the importance of PDE components. Further, it is observed that Unisolver significantly outperforms FNO under complex conditions, such as smaller ν and larger ω , particularly in OOD conditions. More showcases can be found in Appendix A.

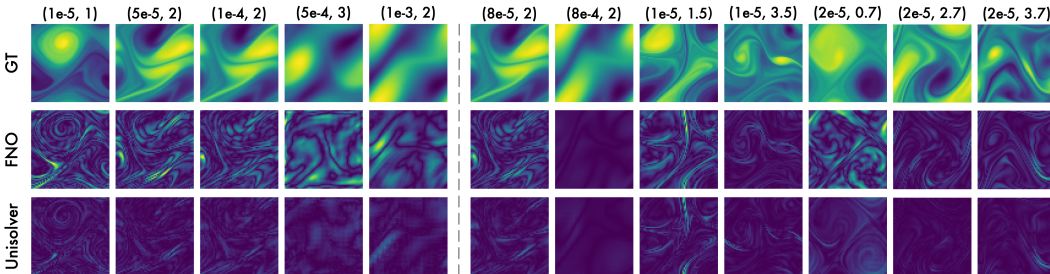


Figure 3: Showcases on error maps of FNO and Unisolver on HeterNS benchmark. All the cases have the same initial condition but different viscosity coefficients and force-frequency coefficients, which are presented in the first row. The left shows ID conditions, while the right depicts OOD conditions.

Scalability Scalability is vital for building a universal PDE solver. Figure 4 illustrates our exploration of Unisolver’s scalability, where we progressively increase the training data by 60 times and the model parameters by 21 times. Unisolver exactly displays the scaling law, achieving better performance with increased data and parameters, posing the potential for a universal PDE solver.

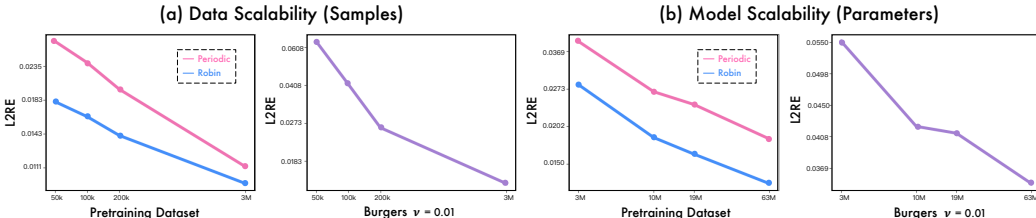


Figure 4: Data scalability (60x) and model scalability (21x) on the PDEformer benchmark. Relative L2 error for pre-training (periodic and Robin) and Burgers equation are plotted on a log-log scale.

5 Conclusions

To break the generalization bottleneck, this paper presents Unisolver as a PDE-conditional Transformer, which stems from the theoretical analysis of the PDE-solving process. Concretely, Unisolver proposes a complete set of PDE components and embeds these components into domain-wise and point-wise deep conditions separately for deep conditions. By integrating these conditions with Transformers through a decoupled mechanism, Unisolver can handle universal PDE components and achieve consistent state-of-the-art results across three challenging, large-scale benchmarks. Extensive analyses are provided to verify the performance, generalizability and scalability of our model.

References

- [1] William F Ames. *Numerical methods for partial differential equations*. Academic press, 2014.
- [2] Vladimir Igorevich Arnol'd. *Mathematical methods of classical mechanics*. Springer Science & Business Media, 2013.
- [3] Johannes Brandstetter, Daniel Worrall, and Max Welling. Message passing neural pde solvers. In *ICLR*, 2022.
- [4] Tom Brown, Benjamin Mann, Nick Ryder, Melanie Subbiah, Jared D Kaplan, Prafulla Dhariwal, Arvind Neelakantan, Pranav Shyam, Girish Sastry, Amanda Askell, et al. Language models are few-shot learners. In *NeurIPS*, 2020.
- [5] Jacob Devlin, Ming-Wei Chang, Kenton Lee, and Kristina Toutanova. Bert: Pre-training of deep bidirectional transformers for language understanding. In *NAACL*, 2019.
- [6] Alexey Dosovitskiy, Lucas Beyer, Alexander Kolesnikov, Dirk Weissenborn, Xiaohua Zhai, Thomas Unterthiner, Mostafa Dehghani, Matthias Minderer, Georg Heigold, Sylvain Gelly, et al. An image is worth 16x16 words: Transformers for image recognition at scale. In *ICLR*, 2020.
- [7] Stefan Elfving, Eiji Uchibe, and Kenji Doya. Sigmoid-weighted linear units for neural network function approximation in reinforcement learning. *Neural networks*, 2018.
- [8] Lawrence C Evans. *Partial differential equations*. American Mathematical Society, 2022.
- [9] Jayesh K Gupta and Johannes Brandstetter. Towards multi-spatiotemporal-scale generalized pde modeling. *TMLR*, 2023.
- [10] Zhongkai Hao, Chang Su, Songming Liu, Julius Berner, Chengyang Ying, Hang Su, Anima Anandkumar, Jian Song, and Jun Zhu. Dpot: Auto-regressive denoising operator transformer for large-scale pde pre-training. In *ICML*, 2024.
- [11] Zhongkai Hao, Chengyang Ying, Zhengyi Wang, Hang Su, Yinpeng Dong, Songming Liu, Ze Cheng, Jun Zhu, and Jian Song. Gnot: A general neural operator transformer for operator learning. In *ICML*, 2023.
- [12] Kaiming He, Xinlei Chen, Saining Xie, Yanghao Li, Piotr Dollár, and Ross Girshick. Masked autoencoders are scalable vision learners. In *CVPR*, 2022.
- [13] Tero Karras, Miika Aittala, Timo Aila, and Samuli Laine. Elucidating the design space of diffusion-based generative models. *NeurIPS*, 2022.
- [14] Diederik P. Kingma and Jimmy Ba. Adam: A method for stochastic optimization. In *ICLR*, 2015.
- [15] Nikola Kovachki, Zongyi Li, Burigede Liu, Kamyar Azizzadenesheli, Kaushik Bhattacharya, Andrew Stuart, and Anima Anandkumar. Neural operator: Learning maps between function spaces with applications to pdes. *JMLR*, 2023.
- [16] Zijie Li, Kazem Meidani, and Amir Barati Farimani. Transformer for partial differential equations' operator learning. *TMLR*, 2023.
- [17] Zijie Li, Dule Shu, and Amir Barati Farimani. Scalable transformer for pde surrogate modeling. In *NeurIPS*, 2024.
- [18] Zongyi Li, Daniel Zhengyu Huang, Burigede Liu, and Anima Anandkumar. Fourier neural operator with learned deformations for pdes on general geometries. *JMLR*, 2023.
- [19] Zongyi Li, Nikola Borislavov Kovachki, Kamyar Azizzadenesheli, Burigede liu, Kaushik Bhattacharya, Andrew Stuart, and Anima Anandkumar. Fourier neural operator for parametric partial differential equations. In *ICLR*, 2021.
- [20] Zongyi Li, Hongkai Zheng, Nikola Kovachki, David Jin, Haoxuan Chen, Burigede Liu, Kamyar Azizzadenesheli, and Anima Anandkumar. Physics-informed neural operator for learning partial differential equations. *J. Data Sci.*, 2021.
- [21] Yuxuan Liu, Zecheng Zhang, and Hayden Schaeffer. Prose: Predicting operators and symbolic expressions using multimodal transformers. *arXiv preprint arXiv:2309.16816*, 2023.
- [22] Ze Liu, Yutong Lin, Yue Cao, Han Hu, Yixuan Wei, Zheng Zhang, Stephen Lin, and Baining Guo. Swin transformer: Hierarchical vision transformer using shifted windows. In *ICCV*, 2021.

- [23] Cooper Lorsung, Zijie Li, and Amir Barati Farimani. Physics informed token transformer for solving partial differential equations. *Mach. Learn.: Sci. Technol*, 2024.
- [24] Ilya Loshchilov and Frank Hutter. Sgdr: Stochastic gradient descent with warm restarts. In *ICLR*, 2016.
- [25] Lu Lu, Pengzhan Jin, Guofei Pang, Zhongqiang Zhang, and George Em Karniadakis. Learning nonlinear operators via deepnet based on the universal approximation theorem of operators. *Nat. Mach. Intell*, 2021.
- [26] Yining Luo, Yingfa Chen, and Zhen Zhang. Cfdbench: A comprehensive benchmark for machine learning methods in fluid dynamics. *arXiv preprint arXiv:2310.05963*, 2023.
- [27] Michael McCabe, Bruno Régaldo-Saint Blancard, Liam Holden Parker, Ruben Ohana, Miles Cranmer, Alberto Bietti, Michael Eickenberg, Siavash Golkar, Geraud Krawezik, Francois Lanusse, et al. Multiple physics pretraining for physical surrogate models. In *NeurIPS AI for Science Workshop*, 2023.
- [28] Taesung Park, Ming-Yu Liu, Ting-Chun Wang, and Jun-Yan Zhu. Semantic image synthesis with spatially-adaptive normalization. In *CVPR*, 2019.
- [29] William Peebles and Saining Xie. Scalable diffusion models with transformers. In *ICCV*, 2023.
- [30] Ethan Perez, Florian Strub, Harm De Vries, Vincent Dumoulin, and Aaron Courville. Film: Visual reasoning with a general conditioning layer. In *AAAI*, 2018.
- [31] Colin Raffel, Noam Shazeer, Adam Roberts, Katherine Lee, Sharan Narang, Michael Matena, Yanqi Zhou, Wei Li, and Peter J Liu. Exploring the limits of transfer learning with a unified text-to-text transformer. 2020.
- [32] Md Ashiqur Rahman, Zachary E Ross, and Kamyar Azizzadenesheli. U-no: U-shaped neural operators. *TMLR*, 2023.
- [33] Maziar Raissi, Paris Perdikaris, and George Em Karniadakis. Physics-informed neural networks: A deep learning framework for solving forward and inverse problems involving nonlinear partial differential equations. *J. Comput. Phys.*, 2019.
- [34] Rajhans Singh, Ankita Shukla, and Pavan Turaga. Polynomial implicit neural representations for large diverse datasets. In *CVPR*, 2023.
- [35] Shashank Subramanian, Peter Harrington, Kurt Keutzer, Wahid Bhimji, Dmitriy Morozov, Michael W Mahoney, and Amir Gholami. Towards foundation models for scientific machine learning: Characterizing scaling and transfer behavior. In *NeurIPS*, 2023.
- [36] Makoto Takamoto, Francesco Alesiani, and Mathias Niepert. Learning neural pde solvers with parameter-guided channel attention. In *ICML*, 2023.
- [37] Makoto Takamoto, Timothy Praditia, Raphael Leiteritz, Daniel MacKinlay, Francesco Alesiani, Dirk Pflüger, and Mathias Niepert. Pdebench: An extensive benchmark for scientific machine learning. *NeurIPS*, 2022.
- [38] Hugo Touvron, Thibaut Lavril, Gautier Izacard, Xavier Martinet, Marie-Anne Lachaux, Timothée Lacroix, Baptiste Rozière, Naman Goyal, Eric Hambro, Faisal Azhar, et al. Llama: Open and efficient foundation language models. *arXiv preprint arXiv:2302.13971*, 2023.
- [39] Hugo Touvron, Louis Martin, Kevin Stone, Peter Albert, Amjad Almahairi, Yasmine Babaei, Nikolay Bashlykov, Soumya Batra, Prajjwal Bhargava, Shruti Bhosale, et al. Llama 2: Open foundation and fine-tuned chat models. *arXiv preprint arXiv:2307.09288*, 2023.
- [40] Ashish Vaswani, Noam Shazeer, Niki Parmar, Jakob Uszkoreit, Llion Jones, Aidan N Gomez, Łukasz Kaiser, and Illia Polosukhin. Attention is all you need. In *NeurIPS*, 2017.
- [41] Hanchen Wang, Tianfan Fu, Yuanqi Du, Wenhao Gao, Kexin Huang, Ziming Liu, Payal Chandak, Shengchao Liu, Peter Van Katwyk, Andreea Deac, et al. Scientific discovery in the age of artificial intelligence. *Nature*, 2023.
- [42] Gege Wen, Zongyi Li, Kamyar Azizzadenesheli, Anima Anandkumar, and Sally M Benson. U-fno—an enhanced fourier neural operator-based deep-learning model for multiphase flow. *Adv. Water Resour.*, 2022.
- [43] Haixu Wu, Tengge Hu, Huakun Luo, Jianmin Wang, and Mingsheng Long. Solving high-dimensional pdes with latent spectral models. In *ICML*, 2023.

- [44] Haixu Wu, Huakun Luo, Haowen Wang, Jianmin Wang, and Mingsheng Long. Transolver: A fast transformer solver for pdes on general geometries. In *ICML, 2024*.
- [45] Zhanhong Ye, Xiang Huang, Leheng Chen, Hongsheng Liu, Zidong Wang, and Bin Dong. Pdeformer: Towards a foundation model for one-dimensional partial differential equations. In *ICLR AI4Differential Equations In Science Workshop, 2024*.
- [46] Chengxuan Ying, Tianle Cai, Shengjie Luo, Shuxin Zheng, Guolin Ke, Di He, Yanming Shen, and Tie-Yan Liu. Do transformers really perform badly for graph representation? *NeurIPS, 2021*.

A More Showcases

We provide more showcases here as a supplement to the numerical results of the main text.

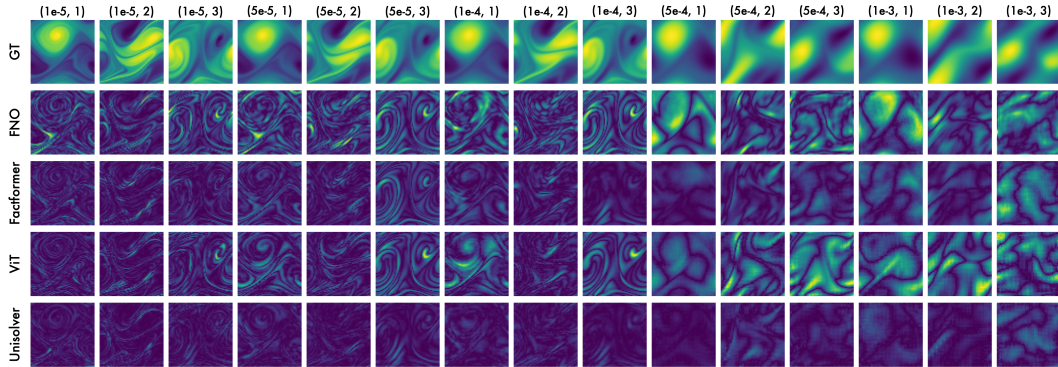


Figure 5: Showcases comparison for in-distribution (ID) data with three baselines on the HeterNS dataset. See Table 3 and 4 for numerical comparison. All data has the same initial condition but different viscosity coefficients and force frequency coefficients, as shown in the first row. Error maps are provided. A darker color indicates a lower error.

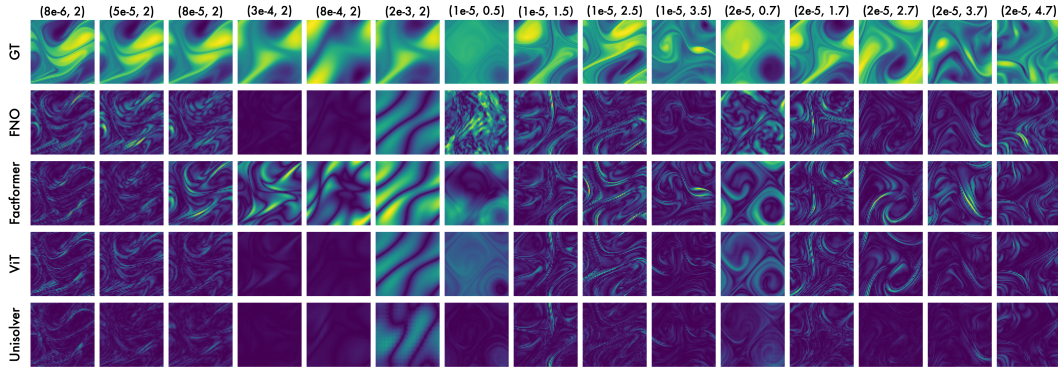


Figure 6: Showcases comparison for out-of-distribution (OOD) data with three baselines on the HeterNS dataset with the same initial conditions but different viscosity coefficients and force frequency coefficients. See Table 3 and 4 for numerical comparison. Error maps are provided. A darker color indicates a lower error.

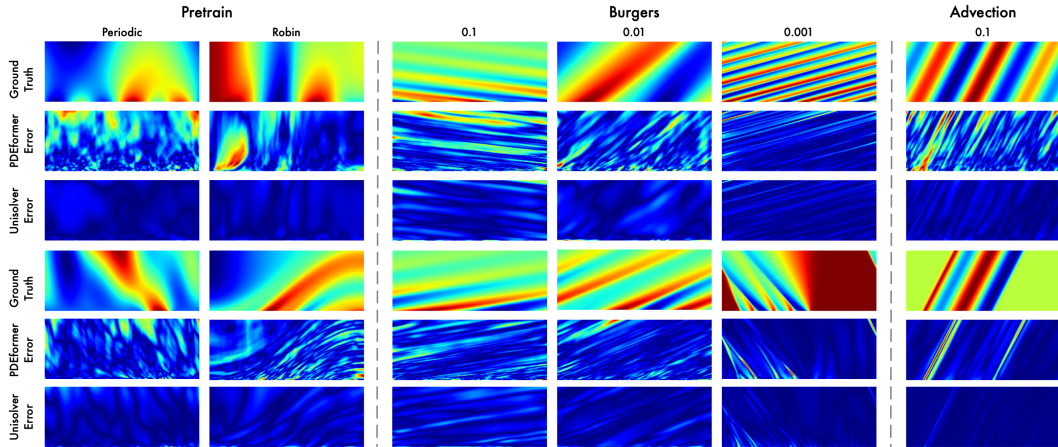


Figure 7: Showcases comparison with PDEformer on the pre-training and downstream tasks of 1D time-dependent PDEs. See Table 5 for numerical comparison. The pre-training dataset contains both periodic and robin boundary conditions. The numbers in the Burgers columns refer to the diffusion coefficient ν and the number in the Advection column indicates the constant advection speed β . Error maps are provided. A darker color indicates a lower error.

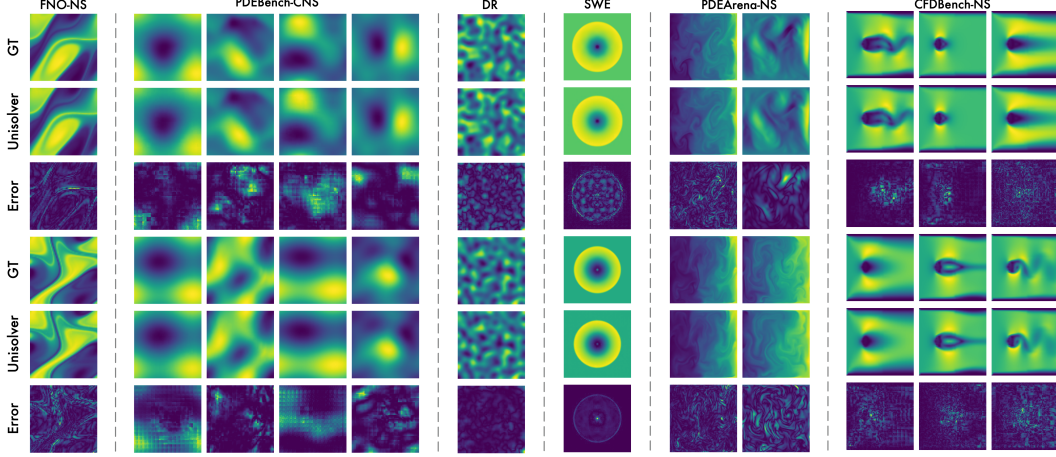


Figure 8: Showcases of Unisolver on 2d mixed PDE benchmark that covers a wide range of PDE components. See Table 6 for numerical comparison with DPOT. Both prediction results and error maps are provided. As shown in the CFDBench-NS columns, Unisolver presents an impressive ability to handle different geometry conditions.

B Analytical Solution for the String Vibration Equation

Here we derive the analytical solution for the PDE (1a) with boundary conditions (1b) and initial conditions (1c).

We extend $\varphi(x)$, $\psi(x)$ and $f(x, t)$ as odd, periodic functions of x with period $2L$, defining $\Phi(x)$, $\Psi(x)$ and $F(x, t)$ as follows:

$$\begin{aligned}
 \Phi(x) &= -\Phi(-x), & \Phi(x) &= \Phi(x + 2L), & -\infty < x < \infty, \\
 \Phi(x) &= \varphi(x), & & & 0 \leq x \leq L, \\
 \Psi(x) &= -\Psi(-x), & \Psi(x) &= \Psi(x + 2L), & -\infty < x < \infty, \\
 \Psi(x) &= \psi(x), & & & 0 \leq x \leq L. \\
 F(x, t) &= -F(-x, t), & F(x, t) &= F(x + 2L, t), & -\infty < x < \infty, 0 \leq t \leq T \\
 F(x, t) &= f(x, t), & & & 0 \leq x \leq L, 0 \leq t \leq T.
 \end{aligned} \tag{4}$$

Thus, we obtain a wave equation defined on the upper half-plane, with initial conditions $\Phi(x)$ and $\Psi(x)$.

$$\begin{aligned}
 \partial_{tt}U - a^2\partial_{xx}U &= F, & (x, t) &\in \mathbb{R} \times (0, T), \\
 U(x, 0) &= \Phi(x), & \partial_t U(x, 0) &= \Psi(x), & x \in \mathbb{R}.
 \end{aligned} \tag{5}$$

Lemma B.1. *The solution of the simplified equation (9) is $U(x, t) = \frac{1}{2a} \int_{x-at}^{x+at} \Psi(\xi) d\xi$.*

$$\begin{aligned}
 \partial_{tt}U - a^2\partial_{xx}U &= 0, & (x, t) &\in \mathbb{R} \times (0, T), \\
 U(x, 0) &= 0, & \partial_t U(x, 0) &= \Psi(x), & x \in \mathbb{R}.
 \end{aligned} \tag{6}$$

Proof. The above expression for U can be derived using the method of operator splitting and characteristic lines.

Note that

$$0 = \partial_{tt}U - c^2\partial_{xx}U = (\partial_t - a\partial_x)(\partial_t + a\partial_x)U.$$

Let

$$V = (\partial_t + a\partial_x)U$$

Then

$$\partial_t V - a\partial_x V = 0, \quad V(x, 0) = \Psi(x).$$

Using the method of characteristic lines for first-order equations, we obtain

$$V(x, t) = V(x + at, 0) = \Psi(x + at).$$

Thus, U satisfies

$$(\partial_t + a\partial_x)U = V = \Psi(x + at).$$

For this first-order equation, along the characteristic line passing through the point (X, T') , defined by $x = at + X - aT'$, we have

$$\frac{du(X - aT' + at, t)}{dt} = \Psi(X - aT' + 2at).$$

By integrating on both sides, we get

$$U(X - aT' + at, t) = \int_0^t \Psi(X - aT' + 2as) ds.$$

Therefore,

$$U(x, t) = \int_0^t \Psi(x - at + 2as) ds = \frac{1}{2a} \int_{x-at}^{x+at} \Psi(\xi) d\xi.$$

It is straightforward to verify it's indeed a solution by substituting it into the equation, given that $\Psi \in C^1(\mathbb{R})$. \square

Inspired by the principle of linear superposition for linear problems, the solution $U = U(t, x)$ for equation (5) can be decomposed as

$$U = U_1 + U_2 + U_3,$$

where U_1, U_2 , and U_3 are the solutions to the following three equations, respectively,

$$\begin{cases} \partial_{tt}U - a^2\partial_{xx}U = 0, \\ U(x, 0) = \Phi(x), \\ \partial_t U(x, 0) = 0, \end{cases} \quad \begin{cases} \partial_{tt}U - a^2\partial_{xx}U = 0, \\ U(x, 0) = 0, \\ \partial_t U(x, 0) = \Psi(x), \end{cases} \quad \begin{cases} \partial_{tt}U - a^2\partial_{xx}U = F(x, t), \\ U(x, 0) = 0, \\ \partial_t U(x, 0) = 0. \end{cases}$$

Lemma B.2. *The three solutions have the following simple relationships. Denoting that $U_2 = S_\Psi$, we have*

$$U_1 = \frac{dS_\Phi}{dt}, \quad U_3 = \int_0^t S_F(\tau, x)(t - \tau, x) d\tau.$$

Proof. These relations can be verified by substitution. \square

Thus, the explicit expression of U is,

$$\begin{aligned} U(x, t) &= (U_1 + U_2 + U_3)(x, t) \\ &= \frac{1}{2}(\Phi(x + at) + \Phi(x - at)) + \frac{1}{2a} \int_{x-at}^{x+at} \Psi(\xi) d\xi + \frac{1}{2a} \int_0^t d\tau \int_{x-a(t-\tau)}^{x+a(t-\tau)} F(\xi, \tau) d\xi \end{aligned}$$

Noting that due to the construction of $\Phi(x)$ and $\Psi(x)$, the solution $U(x, t)$ of equation 5 is an odd function of x with a period of $2L$. Moreover, it satisfies $U(kL, t) = 0, \forall k \in \mathbb{Z}, t \in \mathbb{R}$, ensuring that the boundary conditions of the original string vibrating equation (1a) are met. Therefore, we obtain the solution of equation (1a):

$$u(x, t) = U(x, t), \quad \forall (x, t) \in [0, L] \times [0, T] \quad (7)$$

C Benchmarks

C.1 HeterNS

Similar to FNO [19], we consider the 2-d Navier-Stokes equation in vorticity formulation for the viscous, incompressible fluid on a unit torus:

$$\partial_t w(x, t) + u(x, t) \cdot \nabla w(x, t) = \nu \Delta w(x, t) + f(x), \quad x \in (0, 1)^2, t \in (0, T] \quad (8a)$$

$$\nabla \cdot u(x, t) = 0, \quad x \in (0, 1)^2, t \in [0, T] \quad (8b)$$

$$w(x, 0) = w_0(x), \quad x \in (0, 1)^2 \quad (8c)$$

We experiment with viscosity $\nu \in [8 \times 10^{-6}, 2 \times 10^{-3}]$ and external force in the form $f(x) = 0.1(\sin(\omega\pi(x_1 + x_2)) + \cos(\omega\pi(x_1 + x_2)))$. Specifically, we pre-train models on a dataset with $\nu \in \{1 \times 10^{-5}, 5 \times 10^{-5}, 1 \times 10^{-4}, 5 \times 10^{-4}, 1 \times 10^{-3}\}$ and $\omega \in \{1, 2, 3\}$, and test the models on both in-domain and out-of-domain equation components. Pretraining dataset can be found here ³.

C.2 1D Time-dependent PDEs

As described in PDEformer [45], this benchmark contains 3 million high equality 1D time-dependent PDEs with various equation components for pre-training and then evaluates the pre-trained model using two downstream tasks from PDEBench, e.g. advection equation and Burgers equation.

Pre-training The pre-training dataset is generated following the PDE family:

$$\partial_t u + f_0(u) + s(x) + \partial_x(f_1(u) - \kappa(x)\partial_x u) = 0, (x, t) \in [-1, 1] \times [0, 1] \quad (9a)$$

$$u(0, x) = g(x), x \in [-1, 1] \quad (9b)$$

where $f_i(u) = c_{i1}u + c_{i2}u^2 + c_{i3}u^3, i = 0, 1$. Each coefficient c_{ik} is set to zero with probability 0.5, and uniformly sampled from $[-3, 3]$ otherwise.

Notably, terms with a zero coefficient will be excluded in the equation symbolic expression embedded by a LLM. The initial condition $g(x)$ is randomly generated within the family of trigonometric functions, which is same as downstream tasks.

This dataset includes both periodic and non-periodic boundary conditions, with 1.5 million samples each. For the non-periodic cases, the boundary condition type at each endpoint are randomly selected from Dirichlet, Neumann, and Robin types. The Dirichlet condition specifies the solution value at the boundary, the Neumann condition specifies the derivative value at the boundary, and the Robin condition is a linear combination of the two, where Dirichlet and Neumann conditions can be seen as corner cases of the Robin condition.

In conclusion, the domain-wise components of the pre-training dataset include equation symbolic expression, boundary condition types, and coefficients of f_i and point-wise components include the force fields $s(x)$ and $\kappa(x)$ and boundary value functions. The input consists of the equation’s initial condition with a resolution of 256 and above classified components, and the output is solution $u(x, t)$ with a resolution of 256×100 .

Downstream tasks We employed the following two 1D PDE datasets from PDEBench as downstream evaluation tasks. All tasks adhere to periodic boundary conditions and the same initial condition family. The resolution of these samples is 1024×201 . For each dataset, we utilize the first 9000 samples for finetuning and the rest 1000 samples for testing. We downsample the spatial resolution of these datasets to 256 and maintain the temporal resolution unchanged. The downstream PDEs consist of the Advection equation and the Burgers equation.

(1) Advection equation The advection equation models pure advection behavior without non-linearity, which can be formalized as:

$$\partial_t u(t, x) + \beta \partial_x u(x, t) = 0, x \in (0, 1), t \in (0, 2] \quad (10a)$$

$$u(0, x) = u_0(x), x \in (0, 1), \quad (10b)$$

where constant advection speed β and equation symbols are domain-wise components in this dataset. The exact solution of the equation is $u(t, x) = u_0(x - \beta t)$. Only the periodic boundary condition is considered. The initial condition uses a super-position of sinusoidal waves as, $u_0(x) = \sum_{k_i=k_1, \dots, k_N} A_i \sin(k_i x + \phi_i)$, where $k_i = 2\pi n_i / L_x$ are wave numbers and $n_i \in \mathbb{N}$ are selected randomly in $[1, n_{max}]$.

³https://drive.google.com/drive/folders/1te5IyQHTznu_Kw7v3zDHg0i_KCHysPKw

(2) Burgers equation This fundamental equation in fluid mechanics models the non-linear behavior and diffusion process of fluid dynamics as

$$\partial_t u(t, x) + \partial_x (u(t, x)^2 / 2) = \nu / \pi \partial_{xx} u(t, x), \quad x \in (0, 1), t \in (0, 2], \quad (11a)$$

$$u(0, x) = u_0(x), \quad x \in (0, 1), \quad (11b)$$

where diffusion coefficient ν and equation formulation are the domain-wise components. To align with the solution domain with pretraining dataset, we rescale the spatial-temporal coordinates (x, t) to $(x', t') \in [-1, 1] \times [0, 1]$. The PDEs after the coordinate transformation are given by:

- Burgers' equation: $\partial_{t'} u + \partial_{x'} (2u^2) - \frac{8\nu}{\pi} \partial_{x'x'} u = 0$, where $t' = \frac{t}{2}, x' = 2x - 1$.
- Advection equation: $\partial_{t'} u + \partial_{x'} (4\beta u) = 0$, where $t' = \frac{t}{2}, x' = 2x - 1$.

C.3 2D Mixed PDEs

This dataset is presented by DPOT [10], which consists of the following 12 datasets from 4 benchmarks. These datasets are aggregated to pre-train a foundational neural PDE solver.

FNO- ν This benchmark considers the 2D Navier-Stokes equation for a viscous, incompressible fluid in vorticity form on the unit torus. The task is to estimate the vorticity field of the future ten timesteps on a regular 64×64 grid based on the initial ten timesteps observations of the vorticity field. The only varying PDE component in this dataset is the viscosity coefficient, which varies in $\{1 \times 10^{-5}, 1 \times 10^{-4}, 1 \times 10^{-3}\}$. We utilize 1000, 9800, and 1000 instances for each viscosity value to pre-train or finetune our model, and use the rest 200 instances to test its performance.

PDEBench The following three datasets are derived from PDEBench, encompassing the compressible Navier-Stokes equation, the diffusion-reaction equation, and the shallow-water equation. All datasets considered in PDEBench adhere to periodic boundary conditions.

(1) The compressible Navier-Stokes equation models compressible fluid dynamics, such as shock wave formation and propagation. In this dataset, two domain-wise components are considered, namely Mach number and shear viscosity. For these two components, this dataset provides four combinations, which are $(1, 0.1), (1, 0.01), (0.1, 0.1), (0.1, 0.01)$. Each combination provides 9000 instances for training and 200 instances for testing. The instances in this dataset take the spatial resolution of 128×128 , and the task is to predict the future 11 timesteps of vorticity, pressure and density given the initial 10 timesteps of observations.

(2) The shallow-water equations, derived from the general Navier-Stokes equations, model free-surface flow problems,

$$\partial_t h + \nabla \cdot (h\mathbf{u}) = 0, \quad (12a)$$

$$\partial_t (h\mathbf{u}) + \nabla \cdot \left(\frac{1}{2} h\mathbf{u}^2 + \frac{1}{2} g_r h^2 \right) = -g_r h \nabla b \quad (12b)$$

where h describes the water depth, b describes a spatially varying bathymetry, g_r describes the gravitational acceleration, and $\nabla \cdot (h\mathbf{u})$ can be interpreted as the directional momentum.

The spatial resolution of this benchmark is 128×128 , and the task is to predict the future 91 timesteps of water depth given the first 10 timesteps of observations.

(3) The 2D Diffusion-Reaction Equation involves two non-linearly coupled variables, namely the activator $u = u(t, x, y)$ and the inhibitor $v = v(t, x, y)$. It is primarily applicable for modeling biological pattern formation.

$$\partial_t u = D_u \partial_{xx} u + D_u \partial_{yy} u + R_u \quad (13a)$$

$$\partial_t v = D_v \partial_{xx} v + D_v \partial_{yy} v + R_v \quad (13b)$$

where $D_u = 1 \times 10^{-3}$ and $D_v = 5 \times 10^{-3}$ are the diffusion coefficient for the activator and inhibitor, respectively, and $R_u = R_u(u, v)$ and $R_v = R_v(u, v)$ are the corresponding reaction functions for the activator and inhibitor, which are defined by the Fitzhugh-Nagumo equation as,

$$R_u(u, v) = u - u^3 - k - v, \quad (14a)$$

$$R_v(u, v) = u - v, \quad (14b)$$

where $k = 5 \times 10^{-3}$. The initial condition is generated as standard normal random noise $u(0, x, y) \sim N(0, 1.0)$ for $x \in (-1, 1)$ and $y \in (-1, 1)$. The dataset is discretized into $N_x = 128$, $N_y = 128$, and $N_t = 101$. The task is to predict the future 91 timesteps of u and v given the initial 10 timesteps of observations.

PDEArena-NS1/2 The velocity function formulation of the incompressible Navier-Stokes equations is very common in real-life applications.

$$\partial_t \mathbf{v} = -\mathbf{v} \cdot \nabla \mathbf{v} + \mu \nabla^2 \mathbf{v} - \nabla p + \mathbf{f}, \quad (15a)$$

$$\nabla \cdot \mathbf{v} = 0 \quad (15b)$$

where $\mathbf{v} \cdot \nabla \mathbf{v}$ is the convection which means the rate of change of \mathbf{v} along \mathbf{v} , $\mu \nabla^2 \mathbf{v}$ is the viscosity, i.e. the diffusion or net movement of \mathbf{v} , ∇p is the internal pressure, and \mathbf{f} is the external buoyancy force. The inclusion of the incompressibility constraint $\nabla \cdot \mathbf{u} = 0$ ensures mass conservation in the Navier-Stokes equations. The spatial resolution is 128×128 . This benchmark contains 2 datasets, one with fixed external force and another with varying external force. Given the initial 10 timesteps of observations, the task on the fixed-force dataset is to predict the future 4 timesteps of velocity, while on the varying-force dataset, the number of timesteps to predict is 46.

CFDBench We consider three important and representative fluid problems that can comprehensively evaluate methods' capabilities to generalize to unseen operating conditions. They are (1) the flow in the lid-driven cavity, (2) the flow into the circular tube, (3) the flow around the cylinder.

$$\partial_t(\rho \mathbf{u}) + \nabla \cdot (\rho \mathbf{u}^2) = -\nabla p + \nabla \cdot \mu(\nabla \mathbf{u} + \nabla \mathbf{u}^T), \quad (16a)$$

$$\nabla \cdot (\rho \mathbf{u}) = 0 \quad (16b)$$

where ρ is the constant density, μ is the dynamic viscosity, $\mathbf{u} = (u, v)^T$ is the velocity field, and p is the pressure. For each problem, flows are generated with different operating parameters, which is the combination of the three kinds of components: (1) the Boundary conditions, (2) the fluid physical properties including the density and the viscosity, and (3) the geometry of the field. The boundary conditions refer to the inlet velocity or the movement velocity according to different cases. Each kind of operating parameter corresponds to one subset. In each subset, the corresponding operating conditions are varied while other parameters remain constant. The task is to predict the future 10 timesteps of velocity given the initial 10 timesteps of observations.

D Implementation Details

D.1 Metrics

Relative L2 for physics fields We can calculate the relative L2 error of model prediction \hat{u} and ground truth u as follows:

$$\frac{\|u - \hat{u}\|_{L^2}}{\|u\|_{L^2}}. \quad (17)$$

where $\|u - \hat{u}\|_{L^2}$ is the L^2 -distance between the predicted solution \hat{u} and the ground-truth solution u , and $\|u\|_{L^2}$ is the L^2 -norm of the ground-truth solution.

Relative Promotion Given the error of our model ϵ_{ours} and the error of the second best model $\epsilon_{\text{second-best model}}$, we can calculate the relative promotion as follows:

$$\text{Relative Promotion} = 1 - \frac{\epsilon_{\text{ours}}}{\epsilon_{\text{second-best model}}}. \quad (18)$$

D.2 Implementations for Each Benchmark

HeterNS As for the HeterNS dataset, the model hyperparameters of the baselines and Unisolver are summarized in Table 8. The count of trainable parameters of each model and the training configurations are already shown in Section 4. For baselines, the viscosity coefficient and the external force are concatenated to the model input along the channel dimension to ensure fair comparison.

Table 8: Model hyperparameters of Unisolver and all baselines on the HeterNS benchmark.

Hyperparameter	Value	Description
FNO		
modes	12	The truncation number of Fourier modes
channels	64	The number of channels in the hidden layers
depths	4	The number of Fourier Layers in the neural network
Factformer		
dim	128	hidden dimension of the transformer
n_head	12	num of attention heads
dim_head	64	hidden dimension of each attention heads
depths	8	The number of Transformer Blocks in the neural network
ViT		
Attention dim	256	The hidden dimension of the transformer attention layer
MLP dim	256	The hidden dimension of the transformer FFN layer
patch_size	4	The height and width of the ViT patches
n_head	8	num of attention heads
dim_head	32	The hidden dimension of each attention heads
depths	12	The number of Transformer Blocks in the neural network
Unisolver		
Attention dim	256	The hidden dimension of the transformer attention layer
MLP dim	256	The hidden dimension of the transformer FFN layer
patch_size	4	The height and width of the Unisolver patches
n_head	8	num of attention heads
dim_head	32	The hidden dimension of each attention heads
depths	8	The number of Transformer Blocks in the neural network

1D Time-dependent PDEs We conduct experiments using the checkpoints and dataset provided by the official repository of PDEformer⁴. We randomly select one subset with periodic boundaries and another subset with Robin boundaries from the pre-training datasets. Both of the subset contain 10,000 samples and are used to calculate the pre-training relative L2 error.

For finetuning on the downstream tasks, we utilize the finetuning script provided in the repository and set the finetuning epochs to 100 for fair comparison. The pre-training and finetuning configurations for our model and the finetuning configurations for PDEformer are shown in Table 10.

As shown in the model scalability experiments in Section 4.4, we progressively increase the Unisolver parameter from 3M to 63M, thus resulting in 4 different model configurations. We present the configurations of these models in Table 9.

2D Mixed PDEs The training hyperparameter and model configurations are presented in Table 11. As this dataset includes multiple distinct PDEs, each accompanied by its unique equation components, we introduce a binary masking channel, where an "1" indicates that the current component is a valid condition and a "0" indicates an invalid component.

Table 9: Model configurations of Unisolver with different sizes.

Parameter Count	Attention dim	MLP dim	Layers	Heads
3M	256	256	6	4
10M	384	384	8	8
19M	512	512	8	8
63M	768	768	12	12

⁴<https://gitee.com/mindspore/mindscience/tree/master/MindFlow/applications/pdeformer1d/>

Table 10: Pre-training and finetuning configurations on the 1D time-dependent PDE benchmark.

Parameter	Value	Description
Unisolver Pre-training		
batch_size	1024	Total batchsize used in one iteration
learning_rate	6e-4	The initial learning rate for the optimizer
epochs	500	The total number of training epochs
loss_type	Relative-l2	Use relative L2-Norm for pretraining
optimizer	Adam	The optimization algorithm
lr_scheduler	Cosine Annealing	The learning rate scheduler
Unisolver Finetuning		
batch_size	256	Total batchsize used in one iteration
learning_rate	1e-5	The initial learning rate for the optimizer
epochs	100	The total number of training epochs
loss_type	Relative-l2	Use relative L2-Norm for finetuning
optimizer	Adam	The optimization algorithm
lr_scheduler	Cosine Annealing	The learning rate scheduler
PDEformer Finetuning		
batch_size	80	Total batchsize used in one iteration
learning_rate	5e-6	The initial learning rate for the optimizer
epochs	100	The total number of training epochs
loss_type	Relative-l2	Use relative L2-Norm for finetuning
optimizer	Adam	The optimization algorithm
lr_scheduler	Cosine Annealing	The learning rate scheduler
warmup_epochs	10	Epochs to linearly increase the learning rate

Table 11: Training configurations on the 2D mixed PDE benchmark.

Parameter	Value	Description
Unisolver Training Configurations		
batch_size	320	Total batchsize used in one iteration
learning_rate	1e-3	The initial learning rate for the optimizer
epochs	1000	The total number of training epochs
loss_type	Relative-l2	Use relative L2-Norm for pretraining
optimizer	AdamW	The optimization algorithm
lr_scheduler	OneCycle	The learning rate scheduler
warmup_epochs	200	Epochs to linearly increase the learning rate
Unisolver Model Configurations		
Attention dim	768	The hidden dimension of the transformer attention layer
MLP dim	768	The hidden dimension of the transformer FFN layer
patch_size	8	The height and width of the ViT patches
n_head	8	num of attention heads
dim_head	96	The hidden dimension of each attention heads
depths	6	The number of Transformer Blocks in the neural network

E Additional Experiments

E.1 OOD Viscosity and OOD External Force

In addition to Table 3 and 4, we further compare the generalizability of Unisolver with other baselines on the both OOD viscosity coefficient and OOD external force of the HeterNS benchmark. Specifically, we generate nine different component pairs (ν, ω) , where ν and ω are both out of the pre-training distribution. The full results are recorded in Table 12.

Table 12: Performance comparison on OOD viscosity ν and OOD force frequency coefficients ω . The pairs in the first row are in the form of (ν, ω) . For clarity, the best result is in bold.

L2RE	(2e-5, 0.7)	(2e-5, 1.7)	(2e-5, 2.7)	(2e-5, 3.7)	(2e-5, 4.7)	(4e-5, 0.8)	(4e-5, 1.4)	(4e-5, 2.3)	(4e-5, 6)
FNO	0.1862	0.0640	0.1176	0.2404	0.4226	0.0873	0.1516	0.0655	1.3102
Factformer	0.2727	0.0735	0.1262	0.3238	0.2868	0.0589	0.1230	0.0495	0.3147
ViT	0.1961	0.0690	0.1075	0.2057	0.2226	0.0488	0.1305	0.0772	0.2276
Unisolver	0.0781	0.0378	0.0471	0.1421	0.1364	0.0399	0.0433	0.0374	0.1431
Promotion	58.06%	40.94%	56.19%	30.92%	38.72%	18.24%	66.82%	24.44%	37.13%

E.2 Hyperparameter Sensitivity

As shown in Table E.2, we test the hyperparameter sensitivity of our model by changing the domain-wise condition ratio α and keeping the other hyperparameters fixed. We pre-train models with domain-wise condition ratios of 0.25, 0.5 and 0.75 on the 1D time-dependent PDE dataset, which contains 50k samples, all adhering to periodic boundary conditions, and report the relative L2 on the pre-training dataset and downstream Burgers dataset with $\nu = 0.001$. In this case, the domain-wise ratio of 0.5 leads to the best results, with the ratio of 0.25 being the worst, which suggests that an appropriate ratio should be chosen in practice.

Table 13: Hyperparameter sensitivity of domain-wise condition ratio.

L2RE	Domain-wise condition ratio		
	0.25	0.50	0.75
Dataset			
PDEformer-50k	0.0331	0.0298	0.0314
Burgers $\nu = 0.001$	0.1127	0.1040	0.1070

E.3 Discussion of Ablation

Why Concat-P is better than ours in pretrain-periodic dataset? Since the periodic boundary does not have the boundary value functions, the model can concentrate on the dominated domain-wise conditions for concatenating the point-wise conditions with model input directly. It is similar to set the domain-wise condition ratio to 1, which is beneficial for learning the complex relations of domain-wise conditions.

E.4 Full Scalability

As a supplement to Figure 4 in the main text, we also conduct experiments on different downstream tasks and record the concrete data in Table 14 for clarity.

Table 14: Scalability results on pre-training dataset and downstream tasks, as depicted in Figure 4.

L2RE	Data Scalability (Samples)				Model Scalability (Parameters)			
	50k	100k	200k	3M	3M	10M	19M	63M
Pretraining Dataset / Circ	0.0282	0.0241	0.0198	0.0112	0.0400	0.0267	0.0241	0.0183
Pretraining Dataset / Robin	0.0181	0.0162	0.0141	0.0099	0.0283	0.0185	0.0162	0.0128
Burgers $\nu = 0.1$	0.0161	0.0116	0.0081	0.0051	0.0143	0.0134	0.0116	0.0091
Burgers $\nu = 0.01$	0.0649	0.0412	0.0260	0.0144	0.0552	0.0421	0.0412	0.0351
Burgers $\nu = 0.001$	0.1399	0.1003	0.0689	0.0299	0.1188	0.0976	0.1003	0.0889

E.5 Detailed Compute Resources

Our models were trained on servers with A100-40G GPUs. Here we present the compute resources needed to reproduce our experiment results in Table 15.

Table 15: Compute resources for each of our benchmarks. For the HeterNS dataset, we report the compute resources needed for all the baselines and our model. For the rest two datasets, we report the compute resources needed for pre-training Unisolver only.

Benchmarks	HeterNS				1D Time-dependent PDEs	2D Mixed PDEs
	FNO	Factformer	ViT	Unisolver	Unisolver	Unisolver
A100 GPU hours	12	100	24	24	3000	800

F Limitations and Future Work

This paper presents Unisolver to solve PDEs under universal PDE components, which achieves impressive performance supported by extensive analyses and visualizations. However, our method is currently limited to grid data due to the patchifying process during the embedding of point-wise components. Actually, this limitation is shared in all the generalizable PDE solvers, such as PDEformer and DPOT. One foundation reason is the lack of suitable and large-scale irregular mesh datasets, which will require extremely high computation costs for generation. Since we mainly focus on the foundation model design in this paper, we would like to leave the mesh dataset as a future work. And the capability to handle irregular meshes of Unisolver can be achieved by replacing the canonical Transformer with the latest geometry-general PDE solver: Transolver [44].